PCCP

RSC Publishing

PAPER

Electron induced reactions of surface adsorbed tungsten hexacarbonyl ($W(CO)_6$)†

Cite this: *Phys. Chem. Chem. Phys.*, 2013, **15**, 4002

Samantha G. Rosenberg, Michael Barclay and D. Howard Fairbrother*

Tungsten hexacarbonyl ($W(CO)_6$) is frequently used as an organometallic precursor to create metal-containing nanostructures in electron beam induced deposition (EBID). However, the fundamental electron stimulated reactions responsible for both tungsten deposition and the incorporation of carbon and oxygen atom impurities remain unclear. To address this issue we have studied the effect of 500 eV incident electrons on nanometer thick films of $W(CO)_6$ under Ultra-High Vacuum (UHV) conditions. Results from X-ray Photoelectron Spectroscopy, Mass Spectrometry, and Infrared Spectroscopy reveal that the initial step involves electron stimulated desorption of multiple CO ligands from parent $W(CO)_6$ molecules and the formation of partially decarbonylated tungsten species ($W_x(CO)_y$). Subsequent electron interactions with these $W_x(CO)_y$ species lead to ligand decomposition rather than further CO desorption, ultimately producing oxidized tungsten atoms incorporated in a carbonaceous matrix. The presence of co-adsorbed water during electron irradiation increased the extent of tungsten oxidation. The electron stimulated deposition cross-section of $W(CO)_6$ at an incident electron energy of 500 eV was calculated to be 6.50×10^{-16} cm^{-2}. When considered collectively with findings from previous precursors ($MeCpPtMe_3$ and $Pt(PF_3)_4$), results from the present study are consistent with the idea that the electron induced reactions in EBID are initiated by low energy secondary electrons generated by primary beam–substrate interactions, rather than by the primary beam itself.

Received 3rd November 2012,
Accepted 30th January 2013

DOI: 10.1039/c3cp43902j

www.rsc.org/pccp

Introduction

Tungsten hexacarbonyl ($W(CO)_6$) is an organometallic precursor widely used to create structurally well-defined, metal-containing nanostructures using electron beam induced deposition (EBID).[1–7] Examples include nanopillars, free-standing wires, and $\approx$1.5 nm nano-dots;[8–10] nanodeposits grown from $W(CO)_6$ have also been used to repair X-ray masks.[11] In the EBID process, typically performed in electron microscopes, deposition is accomplished by irradiating a sample with a tightly focused electron beam in a low vacuum environment that contains a partial pressure of a suitable precursor.[12–15] Deposition occurs when the electron beam decomposes transiently adsorbed precursor molecules into non-volatile fragments. As a strategy for nanofabrication, EBID (also referred to as focused electron beam induced processing, FEBIP) enjoys a combination of unique attributes. These include the ability to prototype free-standing, three-dimensional structures with high spatial resolution without some of the drawbacks of ion implantation (*e.g.* less amorphization and no ion implantation)[16–18] or the need for resist layers, etching steps, or pattern transfer.

One of the principal drawbacks of EBID, however, is the purity of the deposits which typically contain organic contaminants, particularly carbon and oxygen.[19] This is especially true for metal-containing deposits created from organometallic precursors such as metal carbonyls (*e.g.* $W(CO)_6$).[2–4,20] These impurities negatively impact properties (*e.g.* resistivity) and function (*e.g.* catalytic activity). One source of these contaminants is from electron induced decomposition of transiently adsorbed water molecules and hydrocarbons, both of which are also often present in electron microscopes at significant partial pressures. The other source of contamination emanates from the electron stimulated decomposition of the ligand architecture surrounding the central metal atom in an organometallic precursor. Thus, characterization of EBID nanostructures created from $W(CO)_6$ typically reveal the presence of oxidized tungsten atoms and amorphous carbon.[2–4,20]

To improve metal content and mitigate the negative effects of contaminant atoms it is important to develop a more detailed understanding of electron interactions with EBID precursors, such as metal carbonyls. A starting point for this type of information has been gas phase studies on isolated

Department of Chemistry, Johns Hopkins University, Baltimore, MD 21218, USA. E-mail: howardf@jhu.edu

† Electronic supplementary information (ESI) available. See DOI: 10.1039/c3cp43902j

precursor molecules where the electron energies can be well defined and controlled. Indeed, motivated by the need to better understand the EBID process at a molecular level, several gas phase studies have recently been conducted on electron interactions with EBID precursors $W(CO)_6$, $Co(CO)_3(NO)$, $MeCpPtMe_3$, and $Pt(PF_3)_4$.[21–24] Results from these studies have been used to determine electron energy dependent cross sections, identify reaction mechanisms, reaction products, and resonance peak positions.

UHV surface science studies on electron interactions with adsorbed precursor molecules represent the next step in terms of systems with increasing complexity but correspondingly greater relevance to the EBID process.[25–30] Part of the increase in complexity arises because, in contrast to gas phase studies, the electron energies involved in reactions of surface bound precursors cannot be controlled due to the production of secondary electrons generated by primary beam interactions with the substrate. Additional issues include the potential to create intermediates, which can also contribute to the overall electron stimulated reaction processes. Despite these added complexities, surface science studies can be conducted under UHV conditions where contaminant gases, often present in electron microscopes, are absent and the low substrate temperatures required to adsorb the precursor (typically <160 K) limit the importance of diffusion and other thermally stimulated processes. Previous UHV surface science studies on electron stimulated reactions with adsorbed metal carbonyls include investigations on $W(CO)_6$, $Mo(CO)_6$, $Ni(CO)_4$, and $Fe(CO)_5$.[31–38] Key findings from these studies have included the observation of electron stimulated CO desorption and the formation of partially decarbonylated metal carbonyls. In the electron stimulated reactions of $Fe(CO)_5$ molecules adsorbed on Au surfaces and exposed to 0–20 eV electrons the initial step was proposed to involve the formation of $Fe(CO)_4^-$, which then reacts with neighboring $Fe(CO)_5$ molecules to eject CO on the way to forming multinuclear iron carbonyls, such as $Fe_2(CO)_8^-$.[33] These partially decarbonylated metal carbonyls were then degraded by further electron exposure. The structure of the adsorbate layer[39] was also found to be important in determining the film's sensitivity to electron induced transformations.[33]

In the present study we have used an array of surface analytical techniques (X-ray Photoelectron Spectroscopy, Mass Spectrometry, and Infrared Spectroscopy) to interrogate the sequence of electron stimulated bond breaking processes that occur within nanometer thick films of $W(CO)_6$ adsorbed on solid substrates at low temperatures under UHV conditions. In contrast to the focused electron beams used in typical EBID experiments films were exposed to 500 eV electrons from a low energy flood gun. This approach is necessary because it allows us to generate a relatively broad and defocused electron beam with a flux that is relatively uniform over the substrate (≈ 1 cm^2), facilitating the use of traditional surface analytical techniques to study the electron stimulated surface reactions.[30] The energy of the incident electrons generated by the flood gun (500 eV) is less than the higher electron energies (typically >5 keV) used to create EBID structures in electron microscopes, although it is still sufficient to generate a cascade of low energy secondary electrons from the substrate.[40]

Experimental

All experiments were performed on nanometer thick films of tungsten hexacarbonyl ($W(CO)_6$) adsorbed onto cooled (~ 160 K) gold substrates under UHV conditions ($P_{base} < 1 \times 10^{-9}$ Torr during experiments). Films were created in two separate UHV chambers. The effect of electron irradiation was studied *in situ* with X-ray Photoelectron Spectroscopy (XPS), and Mass Spectrometry (MS) in one chamber and Reflective Absorption Infrared Spectrometry (RAIRS) in a second chamber.

Precursor

Tungsten hexacarbonyl ($W(CO)_6$; CAS 14040-11-0, Strem Chemicals, Inc.) exists as a stable white crystal at standard temperature and pressure (STP). The precursor was attached to a stainless steel gas manifold, which was coupled to the UHV chamber *via* a leak valve. The manifold was evacuated and used to pump on the precursor directly. The gas manifold was then filled with a partial pressure of $W(CO)_6$ by heating the precursor and the manifold to ≈ 75 °C.

Substrates

All XPS and MS experiments were conducted on a polycrystalline Au substrate, except for one experiment performed on an amorphous carbon (a:C) substrate which was created by Ar^+ sputtering highly ordered pyrolytic graphite (HOPG). For all RAIRS experiments a polished Au mirror was used as the substrate. Polycrystalline Au was chosen because of its relative ease of cleaning, lack of spectral overlap with any of the prominent W, C, or O XPS transitions, and reflectivity (when polished). Substrates were mounted onto manipulators which have capabilities for *xyz* translation and rotation, as well as the ability to be liquid nitrogen cooled and resistively heated. In the chamber with XPS and MS the polycrystalline Au substrate was cleaned by ion sputtering with 4 keV Ar^+ (>1 h). In RAIRS experiments the polycrystalline Au was polished to increase reflectivity but could not be cleaned in vacuum.

Creating films

Each film was created by leaking $W(CO)_6$ into the chamber through an UHV compatible leak valve and onto a cooled Au substrate. A substrate temperature of ≈ 160 K was used to ensure deposition of the parent compound under UHV conditions and minimize the likelihood of any thermal reactions or decomposition processes upon adsorption; thus ensuring that the experimental data reflects only electron stimulated processes involving $W(CO)_6$ molecules. A substrate temperature of ≈ 160 K was also chosen because it was sufficiently high to prevent the co-adsorption of residual water vapor.[41] In contrast, on the (a:C) substrate a substrate temperature of 100 K was used to promote the co-adsorption of water from the background. In the UHV chamber equipped with MS and XPS, nanometer thick films of $W(CO)_6$ (1.3–1.5 nm) were created

on 1 cm^2 substrates. In these studies, the film thickness was determined by measuring the signal attenuation from the substrate's (Au(4f) or C(1s)) photoelectrons by XPS; an inelastic mean free path of 2.0 nm was used for the C(1s) and Au(4f) photoelectrons.[42] Film thicknesses were converted to monolayer coverages based on the structure of $W(CO)_6$ and were controlled to correspond to average coverages of $\sim$1–2 monolayers. In RAIRS experiments, film thicknesses were not determined quantitatively and were measured in terms of the nominal $W(CO)_6$ exposure as recorded by a nude ion gauge.

Electron source

Once the film's thickness and composition were determined it was exposed to a known electron dose. For all MS and XPS experiments a commercial flood gun (Specs FG 15/40) was used as a broad beam electron source. For RAIRS experiments a home built electron gun, designed from specifications provided in ref. 43 was used as a broad beam electron source.[43] For both electron sources the beam was initially characterized by: (i) a Faraday cup to ensure that the sample surface was subjected to a relatively uniform electron flux and, (ii) a hemispherical electron analyzer to verify the incident electron energy. Both sources were thoroughly outgassed prior to use so as to avoid unwanted deposition onto the sample during electron irradiation. An incident electron energy of 500 eV was used throughout; calculated from the sum of the electron energy generated by the flood gun (480 eV) and a positive bias (+20 V) applied to the substrate to attract secondary electrons emitted during irradiation. The target current was held at 5 μA, monitored by a picoammeter connected to the substrate through the heating rods. For all XPS and MS experiments, electron irradiation is reported in terms of dose (e^- per cm^2). For RAIRS experiments electron dose is reported in terms of irradiation time due to uncertainties in the nature of the surface and the thickness of the adsorbate layer. For these reasons RAIRS experiments provide a qualitative guide to the influence of electron irradiation on $W(CO)_6$ films while XPS and MS measurements can be interpreted quantitatively.

Analytical techniques

X-ray photoelectron spectroscopy. XPS was performed using Mg Kα X-rays ($h\nu$ = 1253.6 eV) and spectra were deconvoluted with commercial software (CASA XPS); peak positions obtained for $W(CO)_6$ films deposited on Au substrates were aligned to the $Au(4f_{7/2})$ peak at 84 eV, while films deposited on (a:C) were aligned to the C(1s) peak at 284.6 eV.[44] All XP spectra were recorded with a step size of 0.125 eV and at pass energies of 22 eV.

Mass spectrometry. A quadrupole mass spectrometer (QMS – Stanford Research System, 0–200 amu) was used to monitor neutral gas phase species produced during electron irradiation as well as the purity of $W(CO)_6$ used to create the films. The QMS was positioned $\sim$10 cm from the substrate and in a direct line-of-sight.

Reflection absorption infrared spectroscopy. RAIR spectra were recorded with a Mattson Infinity Series FTIR by passing the beam through differentially pumped ZnSe windows. Spectra were recorded with a narrow band InSb detector (1900–4000 cm^{-1}), operating at a resolution of 4 cm^{-1}.

The overall experimental approach in this study relied principally on XPS and MS to provide complementary information on the effect that electron exposure has on thin nanometer thick layers (1–2 ML) of $W(CO)_6$. XPS was used to interrogate the electron induced changes that occur to the surface composition and bonding within the adsorbate layer, while MS identified volatile neutral gas phase species produced by electron irradiation. By combining XPS and MS data, changes that occur to the surface layer could be correlated with the production of gas phase species. Infrared Spectroscopy was used in a more qualitative way to: (i) confirm that prior to irradiation the adlayer is composed exclusively of $W(CO)_6$ and, (ii) probe the effect of electron irradiation on bonding within the film, based on changes within the CO stretching region. It should be noted that no attempt has been made to directly correlate the electron dose dependent evolution of RAIR spectra with XPS and MS data due to differences in the nature and cleanliness of the substrates used and the different electron guns employed in the two chambers. Thus, correlations between RAIR spectra and XPS and MS spectra are expressed qualitatively in terms of the effect of increasing electron dose. Quantitative reports of electron dose are restricted to XPS and MS experiments. These represented the majority of studies conducted on well-defined substrates under conditions where film thicknesses could be accurately determined.

Results

Fig. 1 shows that at the lowest $W(CO)_6$ exposures (0.25 L) the background subtracted RAIR spectrum exhibits a single peak centered at 1987 cm^{-1}, very close to the value measured for the only IR active CO stretching mode (T_{1u}) of $W(CO)_6$ which has been reported at 1997 cm^{-1} in the gas phase (Q-branch),[45,46] at 1990 cm^{-1} in solution and between 1985–1992 cm^{-1} in inert gas matrices.[47–50] This supports the idea that prior to electron irradiation the adsorbed layer is composed exclusively of molecular $W(CO)_6$.

As the $W(CO)_6$ exposure increases the peak at 1987 cm^{-1} blue shifts to $\approx$2010 cm^{-1}, saturating in intensity at $\approx$5.0 L. For $W(CO)_6$ exposures in excess of 1.0 L a second IR peak appears at $\approx$2020 cm^{-1}, which also blue shifts to $\approx$2030 cm^{-1} and then increases in intensity as the $W(CO)_6$ exposure increases. The spectral evolution of the CO stretching region shown in Fig. 1 is analogous to the coverage dependent CO stretch of $Cr(CO)_6$ adsorbed on Cu(100) and Pd(100), observed with RAIRS by McCash *et al.*[51,52] In this system a single band is initially observed at $\approx$2000 cm^{-1} which blue shifts to $\approx$2020 cm^{-1} as the coverage increases, accompanied by the appearance of a new band at 2030 cm^{-1}.

Based on the studies of McCash *et al.*[51,52] as well as Rowntree *et al.*, who conducted a detailed RAIRS study of the structure of $Fe(CO)_5$ on Au(111),[39] we can assign the lower frequency band to a disordered monolayer state of $W(CO)_6$ and the higher frequency peak that appears at higher $W(CO)_6$

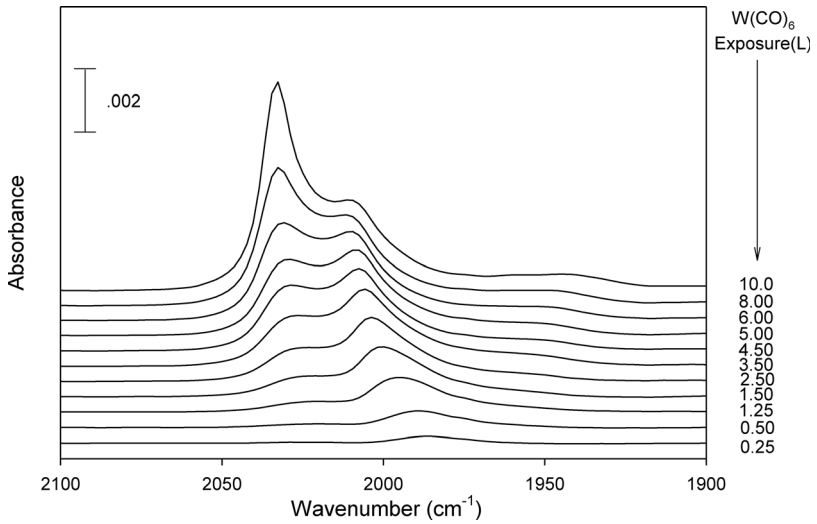

Fig. 1 Evolution of the CO stretching region as a function of $W(CO)_6$ exposure. Adsorption occurred onto a gold mirror at 160 K.

coverages to a more ordered multilayer state representative of $W(CO)_6$ in the solid phase. In these previous RAIRS studies the metal carbonyls were diluted in inert gas matrices to show that the blue shifts in frequencies that occur within each one of the two bands as the $W(CO)_6$ coverage increases are due to repulsive intermolecular dipole–dipole coupling interactions caused by the simultaneous oscillations of the surrounding dipole moments. This type of phenomena is prevalent for strong IR adsorbers, such as the symmetric stretch of metal carbonyls.[39,52,53] Consistent with this argument, the frequency observed at the lowest $W(CO)_6$ coverages, in the present study where there are no intermolecular effects, is closest to the peak position observed for $W(CO)_6$ in other isolated situations (*e.g.* gas phase or inert gas matrices).[45–50]

Fig. 1 is also important for what it does not show. There is no evidence of any spectral features at lower wavelengths ($< \approx 1980\ cm^{-1}$) due to partially decarbonylated species formed by decomposition of $W(CO)_6$. For example, $W(CO)_5$ has its most intense IR band between 1960–1970 cm^{-1} as well as a lower intensity feature at around 1940 cm^{-1}.[48] There is also no evidence of any isolated CO molecules adsorbed on the Au surface which produce a peak above 2050 cm^{-1}.[54] Based on previous Temperature Programmed Desorption (TPD) studies CO is expected to desorb from Au surfaces at substrate temperatures of ≈ 160 K.[55,56] The absence of any CO adsorption on Au was confirmed in the present investigation by conducting separate XPS experiments which showed that exposing a sputter cleaned polycrystalline Au foil at 160 K to comparatively large CO exposures (240 L) did not produce any spectral features within either the C(1s) or O(1s) regions.

The evolution of the CO stretching region in a $W(CO)_6$ film (created by an initial exposure of 5–6 L) exposed to 500 eV electrons is shown in Fig. 2. For very short irradiation times the intensity of the two spectral features above 1985 cm^{-1} decreases,

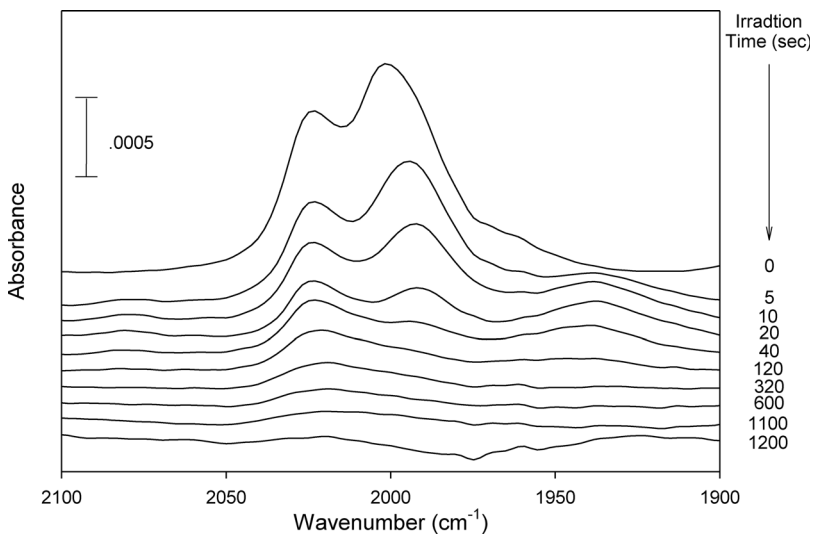

Fig. 2 Effect of electron dose (500 eV incident electrons) on the CO stretching region of a $W(CO)_6$ film adsorbed on a gold substrate at 160 K.

accompanied by the appearance of a broader feature centered at $\approx$1940 cm^{-1}. For more prolonged electron exposures the RAIR spectra shows that all IR bands decrease in intensity until the CO region is essentially featureless. It should also be noted that during electron irradiation no new IR features were observed in the remainder of the spectral window accessible to the InSb detector ($>\approx$1900 cm^{-1}).

The monotonic decrease in intensity of the spectral features above 1985 cm^{-1} indicates that electron irradiation depletes the concentration of $W(CO)_6$, although this effect could be a consequence of either electron stimulated reactions or desorption. An unambiguous determination of which process dominates cannot be made from IR measurements alone. The appearance of new IR features red shifted compared to the $W(CO)_6$ peaks is consistent with the production of partially decarbonylated species; based on matrix isolation and flash photolysis studies the peak positions of any $W(CO)_x$ ($x < 6$) species would be expected to occur 0–150 cm^{-1} below those of the parent compound.[50,57] Fig. 2 also shows that these partially decarbonylated species are not only produced by electron irradiation but also subject to electron stimulated depletion based on their intensity variation as a function of electron irradiation time. Qualitatively these conclusions are similar to the ones reported by Hauchard and Rowntree in a RAIRS study on the effect of low-energy (0–20 eV) electrons on $Fe(CO)_5$ adsorbed on Au(111) who observed that partially decarbonylated species being created with wide and unstructured IR absorbances at lower frequencies than those of the parent molecule.[33] In this study, these new decarbonylated iron species were themselves also subject to electron stimulated reactions analogous to the observations in the present study.

Fig. 3(a) and (b) show the evolution in the W(4f), C(1s) and O(1s) regions for 1.3–1.5 nm thick $W(CO)_6$ films as a function of increasing electron dose. Initial control studies were done to determine the sensitivity of the adlayer to the effects of secondary electrons produced by the X-rays. Results from these studies, shown in Fig. S1 (ESI†), reveal that the spectral envelopes remain relatively unchanged for X-ray exposures $<$100 minutes, except for a slight broadening of the spectral features and small decrease in intensity within the C(1s) and O(1s) regions. For prolonged X-ray irradiation times (>100 min) a small peak associated with graphitic carbon appears at 284.7 eV. Despite this relative insensitivity to X-ray irradiation, which is consistent with observations of Zaera,[58] we minimized any X-ray induced effects on the data shown in Fig. 3 by conducting XPS analysis only on the deposited film and then after a single electron dose. This corresponded to a total X-ray irradiation time of the "as deposited" and irradiated films of $\approx$102 min. After XPS analysis the sample was sputter cleaned. Thus, the data shown in Fig. 3 is the result of multiple experiments performed on different $W(CO)_6$ films with comparable initial thicknesses.

Fig. 3(a) focuses on the effects of comparatively small electron doses ($<7 \times 10^{16}$ e^- per cm^2) on adsorbed $W(CO)_6$ molecules. Prior to electron irradiation the W(4f) region is composed of two peaks, centered at 32.1 eV and 34.3 eV, associated with a $W(4f_{7/2}{:}4f_{5/2})$ doublet; the binding energy of the $W(4f_{7/2})$ peak is consistent with previous reported values for molecular $W(CO)_6$.[58] For the comparatively small electron doses in Fig. 3(a) there is little or no change in the W(4f) region, except for a slight broadening to higher binding energies. Analysis of the integrated area within the W(4f) region reveals that no W atoms are lost from the surface as a result of electron exposure; in other words there is no electron stimulated $W(CO)_6$ desorption. Consequently, all of the transformations observed by XPS and MS can be ascribed to the effects of electron stimulated reactions. Prior to electron irradiation the C(1s) region is composed of two peaks, centered at 287.8 eV and 293.1 eV. The lower binding energy peak can be ascribed to the C(1s) peak of CO ligands in a metal carbonyl such as $W(CO)_6$, while the higher binding energy peak is a shake up feature whose position and relative intensity both occur as a consequence of the fact that in molecular $W(CO)_6$ the CO ligands are in a highly symmetric environment.[58,59] For electron doses $<7 \times 10^{16}$ e^- per cm^2 Fig. 3(a) shows that there are significant changes within the C(1s) region, dominated by a measureable decrease in intensity of the two peaks at 287.75 eV and 293.1 eV. These losses in spectral intensity are accompanied by the appearance of a small peak at 284.7 eV, which becomes more pronounced with increasing electron dose and can be attributed to graphitic like carbon.[44] It should be noted that the binding energy of the C(1s) peak associated with CO species decreases to lower values after electron irradiation (decreasing from a value of 287.8 eV prior to irradiation to 286.4 eV). Such as decrease in binding energy is consistent with the conversion of CO ligands in a discrete metal carbonyl (*i.e.* $W(CO)_6$) to CO molecules adsorbed onto metal (*i.e.* tungsten) atoms or a metal surface.

Analogous to the C(1s) region, the O(1s) spectral envelope prior to electron exposure is composed of two prominent peaks centered at 534.2 eV and 540 eV that can be ascribed to the O(1s) transition of adsorbed CO species and a higher binding energy shake up feature, respectively.[58,59] The peak position and relative intensity of the shake up feature in the O(1s) region is also indicative of CO molecules in the highly symmetric, molecular $W(CO)_6$ parent compound.[59] Upon electron exposure the dominant changes within the O(1s) region are also analogous to those observed in the C(1s) region; notably a significant decrease in intensity of the two original peaks observed upon $W(CO)_6$ deposition, accompanied by the appearance of a new, lower binding energy feature at $\approx$532 eV for the larger electron doses shown in Fig. 3(a). The peak position of this new feature is consistent with the formation of an oxide species (O^{2-}(ads)).[44] It is also worth noting that the effect of 500 eV electrons for these comparatively small electron doses mirrors that of prolonged X-ray irradiation; thus, a comparison of Fig. 3(a) and Fig. S1 (ESI†) reveal that the W(4f), C(1s) and O(1s) regions observed after an electron dose of 3.12×10^{16} e^- per cm^2 are comparable to those observed in Fig. S1 (ESI†) for a $W(CO)_6$ film exposed to 357 minutes of total X-ray irradiation time.

Fig. 3(b) details the effects of electron doses in excess of 7×10^{16} e^- per cm^2 on $W(CO)_6$ films. For comparison the bottom spectra shows the native spectra of $W(CO)_6$ prior to

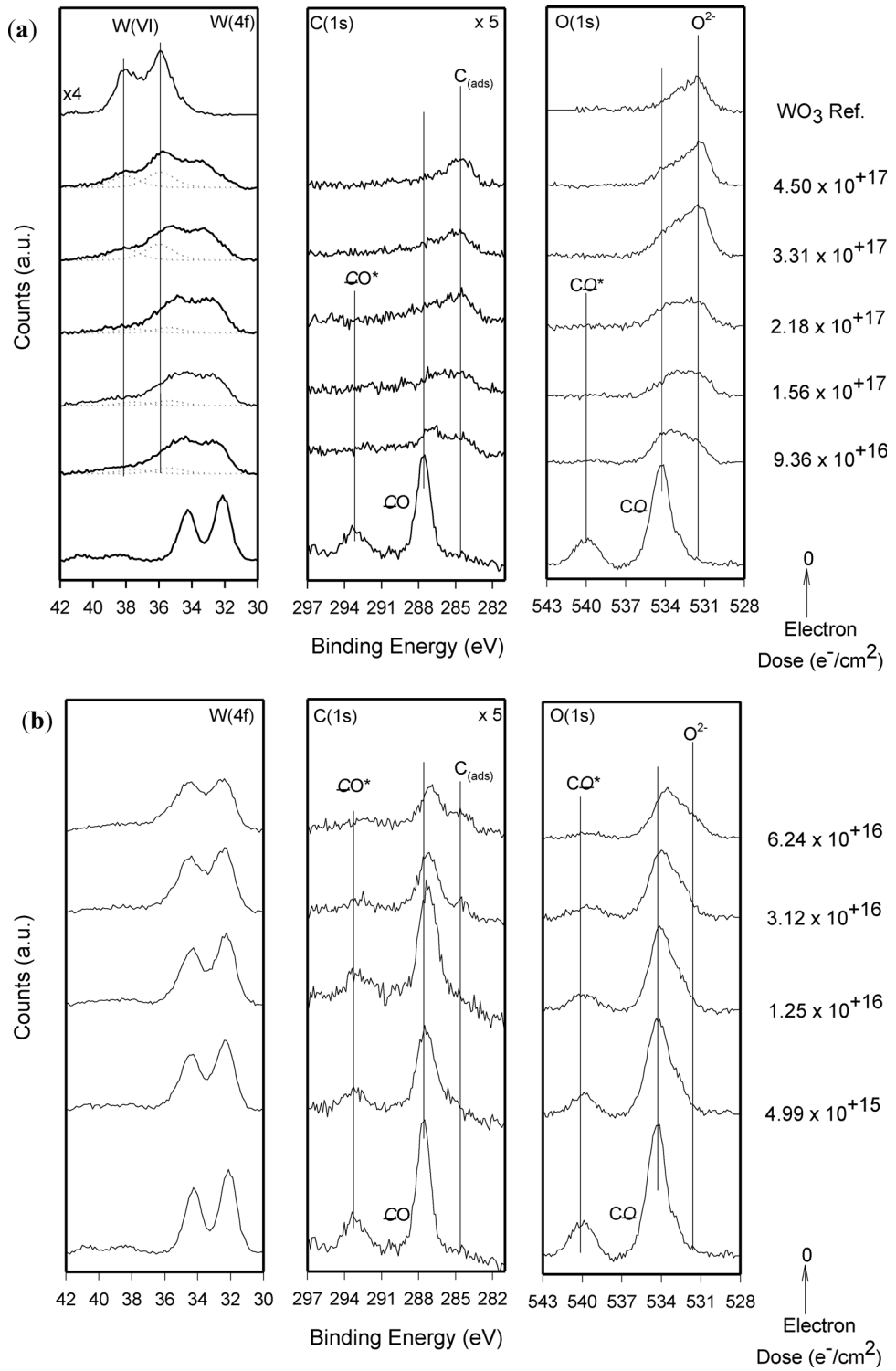

Fig. 3 (a) and (b) Show the evolution of the W(4f), C(1s), and O(1s) XP regions for 1.3–1.5 nm thick films of $W(CO)_6$ irradiated with 500 eV electrons; the corresponding electron dose is shown on the right hand side of each set of W(4f), C(1s), and O(1s) spectra. In (b) a XP reference spectrum of sputter deposited WO_3 is shown.

electron exposure, while the uppermost spectra in the W(4f) and O(1s) regions is a sputter deposited WO_3 sample analyzed with the same XPS system. In contrast to the situation in Fig. 3(a) the W(4f) envelope changes markedly as the electron dose increases above 7×10^{16} e^- per cm^2, broadening by >2 eV to higher binding energies. As part of the spectral transformation within the W(4f) region a new doublet with peaks centered at 36 and 38.1 eV is observed whose intensity increases with

increasing electron dose. Based on a comparison of the sputter deposited reference sample shown in Fig. 3(b) these new peak positions are consistent with the production of W(VI) species in WO_3.[60] Analysis of the C(1s) region shows that for an electron dose of 9.36×10^{16} e^- per cm^2 there is no observable remaining spectral intensity that can be associated with the shake up feature at ≈293 eV and the spectral envelope consists of peaks associated with CO species and graphitic carbon in roughly equal proportion. Fig. 3(b) shows that there is a systematic loss in intensity of the CO peak and a corresponding increase in the surface coverage of graphitic carbon for electron doses in excess of 9.36×10^{16} e^- per cm^2. No evidence was found for carbide formation, based on the absence of a peak in the C(1s) region at a binding energy of ≈283.5 eV.[61–63]

In many ways changes in the O(1s) region for electron doses in excess of 9.36×10^{16} e^- per cm^2 again mirror those observed in the C(1s) region. Thus, for an electron dose of 9.36×10^{16} e^- per cm^2 there is essentially no observable spectral intensity associated with the shake up feature associated with the hexacarbonyl at ≈540 eV. The remaining spectral envelope consists of a single broad feature that consists of residual CO groups with a peak centered just above 534 eV as well as a contribution from the new irradiation induced surface oxide feature at ≈532 eV. As the electron dose increases (to values greater than 9.36×10^{16} e^- per cm^2) the O(1s) region continues to evolve until, for electron doses in excess of 3.31×10^{17} e^- per cm^2, it closely resembles that of the WO_3 reference. For electron doses in excess of ≈3.50×10^{17} e^- per cm^2 the W(4f), C(1s) and O(1s) regions remained relatively constant. Thus, Fig. 3(b) reveals that the ultimate effect of 500 eV electrons on adsorbed $W(CO)_6$ is to produce oxidized tungsten atoms embedded in a carbonaceous matrix. This is qualitatively consistent with compositional data acquired from EBID experiments where $W(CO)_6$ was used as the precursor.[2–4,20]

Fig. 4 shows the variation in the integrated spectral intensity within the C(1s) and O(1s) regions for electron doses $<2.5 \times 10^{17}$ e^- per cm^2. Each data point represents the area after irradiation, normalized to the value measured for the $W(CO)_6$ film prior to electron exposure. Qualitatively, the C/C_0 and O/O_0 plots exhibit similar variations, decreasing in intensity for electron doses $<1 \times 10^{17}$ e^- per cm^2 and remaining relatively constant thereafter. However, the extent to which the carbon and oxygen areas decrease in intensity differs somewhat, with C/C_0 and O/O_0 values falling to ≈55 (±8)% and ≈65 (±7)% of their initial values, respectively.

In Fig. 5 the variation in the fractional concentration of W(VI) atoms is plotted as a logarithmic function of electron dose. The contribution of W(VI) atoms to the overall W(4f) spectral envelope was determined by using the peak positions and peak shapes determined from the WO_3 reference spectrum shown in Fig. 3(b). Accurate peak fitting was facilitated by the fact that the highest binding energy feature observed in the W(4f) region at 38.1 eV can be unambiguously assigned to the $W(4f_{5/2})$ peak of WO_3 (see Fig. 3(b)). Results of this analysis reveal that the fraction of W atoms present as WO_3 becomes appreciable only for electron doses in excess of 1×10^{17} e^- per cm^2 but increases

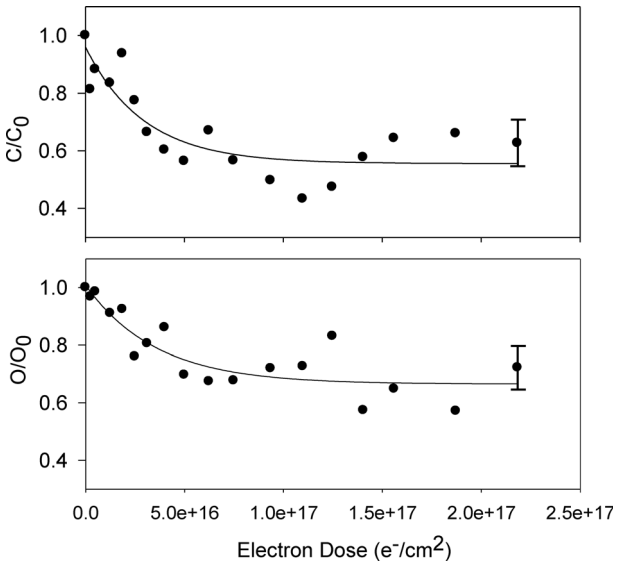

Fig. 4 Effect of electron dose on the relative concentration of (a) carbon and (b) oxygen atoms for 1.3–1.5 nm $W(CO)_6$ films as determined by XPS (incident electron energy 500 eV). Each relative concentration (C/C_0 and O/O_0) is computed with reference to the value measured prior to electron irradiation. The solid lines represent best fits based on first order decay processes.

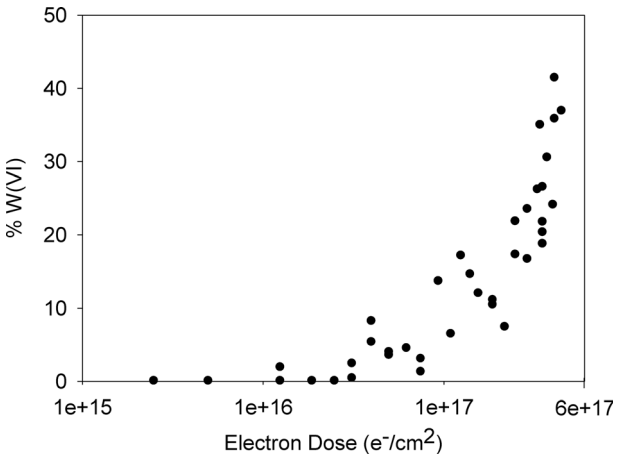

Fig. 5 Effect of electron dose, plotted on a logarithmic scale, of the percent W(VI) determined by XPS peak fitting the W(4f) region.

rapidly thereafter, reaching ≈40% for the largest electron doses (≈5×10^{17} e^- per cm^2).

Fig. 6 illustrates the effect that co-adsorbed water has on the oxidation of W atoms during electron irradiation. The uppermost spectrum corresponds to the W(4f) region of the WO_3 reference, while the lowermost spectrum shows the W(4f) region of a $W(CO)_6$ film after an electron dose of 4.50×10^{17} e^- per cm^2. The middle spectrum is the W(4f) region of a $W(CO)_6$ film exposed to the same electron dose but in the presence of a 0.5–1.0 nm thick film of co-adsorbed water. This experiment was conducted at a lower substrate temperature (100 K) on an (a:C) substrate where residual water vapor in the chamber was co-adsorbed onto the surface. This was confirmed by the appearance of a noticeable increase in the spectral

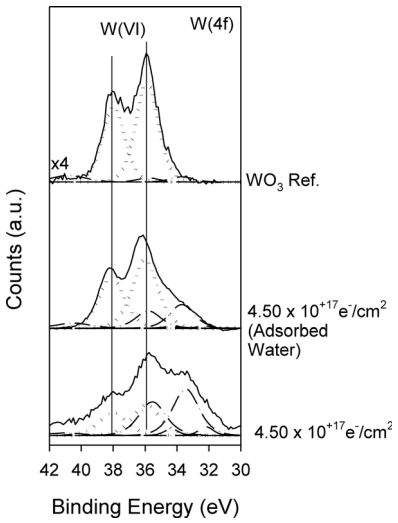

Fig. 6 Effect of co-adsorbed water on the production of W(VI). (a) XP spectrum of a $W(CO)_6$ film adsorbed onto a Au substrate at 163 K after exposure to an electron dose of $4.50 \times 10^{+17} e^-$ per cm^2. (b) XP spectrum of a $W(CO)_6$ film co-adsorbed with H_2O on an (a:C) substrate at 100 K after exposure to an electron dose of $4.50 \times 10^{+17}$ e^- per cm^2. (c) XP reference spectrum of WO_3.

intensity within the O(1s) region. Analysis of the W(4f) region reveals that the proportion of tungsten atoms that become fully oxidized to WO_3 during electron irradiation increases to 71% in the presence of co-adsorbed water. This is approximately double the $\%WO_3$ (37%) observed in the absence of co-adsorbed water.

Fig. 7 examines the nature and kinetics of the neutral gas phase species evolved during electron irradiation of adsorbed $W(CO)_6$. An examination of Fig. 7(a) reveals that CO is the overwhelming gas phase species produced with a dominant peak at 28 due to CO^+ accompanied by smaller daughter ions at 16 (O^+) and 12 (C^+). A much smaller peak is also observed at 44 that can be ascribed to CO_2. The finding that CO is the dominant species evolved is consistent with the results of Friend *et al.* who studied the effect of electron irradiation on $W(CO)_6$ films adsorbed on Si surfaces.[64]

The kinetics of CO evolution were probed by monitoring the initial intensity of CO produced from $W(CO)_6$ films which had been pre-exposed to different electron doses. We previously developed this approach to study the electron stimulated evolution of PF_3 from $Pt(PF_3)_4$.[25] The protocol for these experiments was as follows: an $\approx$1.5 nm thick $W(CO)_6$ film was first exposed to an initial electron dose (the ''pre-irradiation dose'' in Fig. 7(b)). The pre-irradiated film was then once again exposed to electron irradiation and the m/z = 28 signal monitored. Thus, each of the four plots shown in Fig. 7(b) represents the CO evolution from $W(CO)_6$ films exposed to different ''pre-irradiation doses''. The advantage of this approach is that the electron stimulated CO desorption kinetics can be followed by monitoring the change in the m/z = 28 signal at the onset of electron irradiation. This approach is more accurate than following the variation in m/z = 28 signal intensity as a function of irradiation time for a single experiment because of the significant residence time of CO in UHV chambers (*i.e.* CO is not easily pumped away). Analysis of Fig. 7 shows that after pre-irradiation doses of 9.98×10^{15} e^- per cm^2 and 2.50×10^{16} e^- per cm^2 the intensity of CO desorption had decreased to $\approx$45% and $\approx$25% respectively compared to the value measured from a $W(CO)_6$ film of comparable thickness which had not been exposed to any pre-irradiation. For a pre-irradiation dose of 1.50×10^{17} e^- per cm^2 the extent of CO desorption was indistinguishable from the background m/z = 28 signal. Thus, electron stimulated CO desorption from $W(CO)_6$ films is complete before the electron dose reaches 1.5×10^{17} e^- per cm^2.

Fig. 8 compares the kinetics of gas phase and surface transformations that occur as a result of electron irradiating $W(CO)_6$ films. Specifically, Fig. 8 shows the effect of electron dose on: (i) the partial pressure of CO evolved (P_{CO}, measured with MS by the initial increase in m/z = 28 peak as shown in Fig. 7(a)) and (ii) the intensity variation of the carbon and oxygen shake up features observed by XPS in Fig. 3 at 293.1 and 540 eV, respectively. Each of these three variables was normalized to the value measured on a native $W(CO)_6$ film which had not been exposed to any electron irradiation. Fig. 8 shows that P_{CO} as well as the intensity of the carbon and oxygen shakeup features all exhibit a similar decrease in intensity as a function of increasing electron dose, with kinetics that can be well fit by a first order decay process. If all of the data is combined then an average rate constant of 3.44×10^{-17} e^- per cm^2 is obtained; the best-fit from this analysis is shown as a solid line in Fig. 8.

Discussion

In summary, our experimental data reveals that the electron stimulated reactions of adsorbed $W(CO)_6$ proceeds in two stages that can be described as ligand (CO) desorption in the first step followed by ligand (CO) decomposition of the remaining ligands.

Stage 1: electron stimulated CO desorption from $W(CO)_6$

In this first step which dominates for electron doses $< \approx 7 \times 10^{16}$ e^- per cm^2, the overall chemical transformation can be represented as:

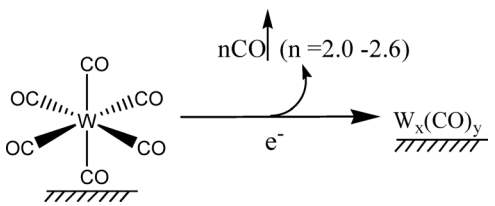

The most direct visual evidence for CO ejection from $W(CO)_6$ comes from the mass spectrometry data shown in Fig. 7. Consistent with the detection of gas phase CO, the XPS data in Fig. 3(a) shows a decrease in intensity of those spectroscopic features within the C(1s) and O(1s) regions associated with the parent molecule. The relationship between the surface coverage of $W(CO)_6$ and gas phase CO production is shown more explicitly in Fig. 8 where it is apparent that the amount of CO

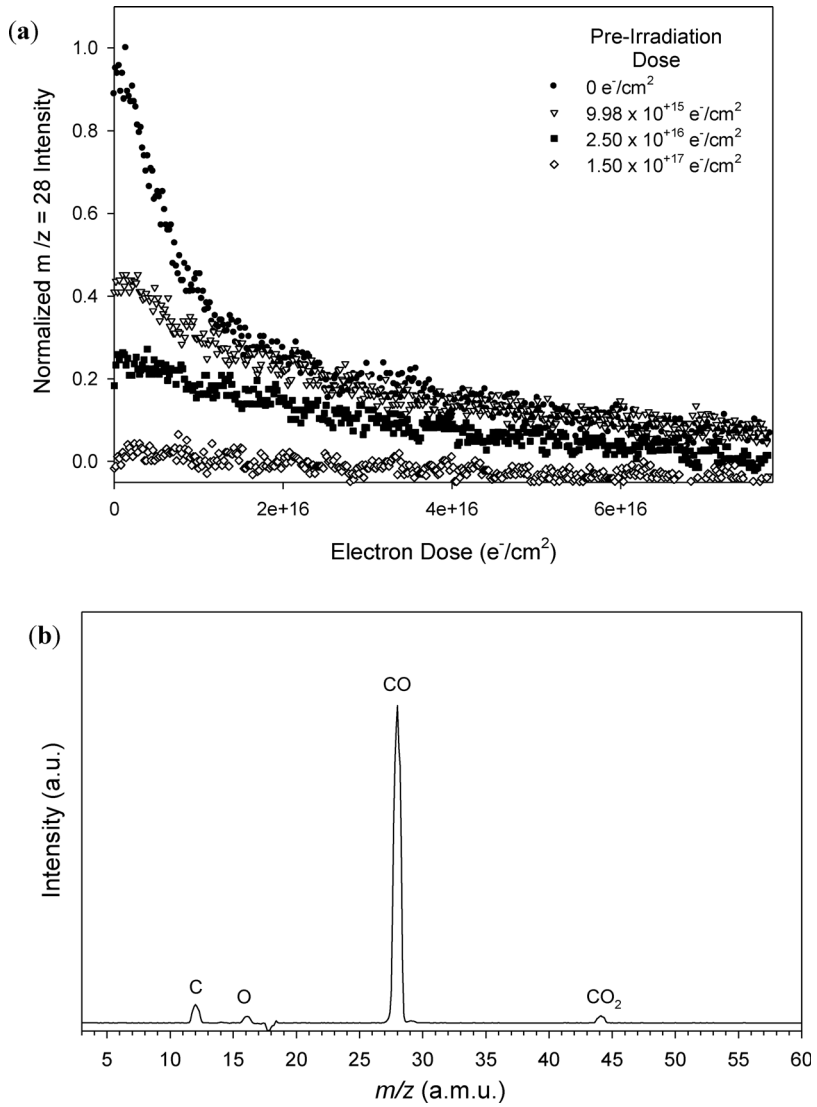

Fig. 7 (a) Mass spectrum (0–60 amu) of the volatile neutral species produced when a ~1.5 nm film of $W(CO)_6$, adsorbed onto a gold substrate at 160 K was irradiated at an electron dose of $5.83 \times 10^{+14}$ e^- per cm^2 and incident energy of 500 eV. The mass spectrum was acquired during the initial (0–20 s) period of irradiation, and background subtracted using the mass spectrum obtained when a sputter clean gold substrate was electron irradiated at the same dose and incident energy. (b) CO produced from electron irradiation of $W(CO)_6$ films pre-irradiated with different electron dose (see text for details).

desorbed scales in direct proportion to the remaining surface coverage of $W(CO)_6$ molecules, the latter measured by the intensity of the C(1s) and O(1s) shake up features.

An important question in the context of EBID is the extent to which species in the precursor's ligand architecture are removed during deposition. For $W(CO)_6$ this is largely a measure of the number of CO ligands that desorb during the first step. This can be determined most directly by measuring the fractional decrease in the carbon and oxygen coverage for electron doses $< \approx 7 \times 10^{16}$ e^- per cm^2, as shown in Fig. 4. Since there are six CO ligands in every $W(CO)_6$ molecule, the changes in the C(1s) and O(1s) areas in Fig. 4(a) and (b) leads to the conclusion that 2.6 and 2 CO molecules desorb, respectively. This difference is most likely a reflection of the difficulty in accurately measuring the integrated area within the C(1s) and O(1s) regions, particularly in using the correct background. A comparison of the C(1s) and O(1s) regions (see Fig. 3) shows that an area analysis in the O(1s) region will be more accurate because of the larger signal intensity and the relatively linear background as compared to the C(1s) region. Consequently, we believe that the average number of CO ligands lost during this first step lies somewhere close to 2. In this respect the electron stimulated decomposition of $W(CO)_6$ differs from two other surface bound EBID precursors we have recently studied ($MeCpPtMe_3$ and $Pt(PF_3)_4$) where the first reaction step involved the cleavage of only one metal–ligand bond ($MeCpPtMe_3(ads) + e^- \rightarrow MeCpPtMe_2(ads) + CH_4\uparrow(g)$; $Pt(PF_3)_4(ads) + e^- \rightarrow Pt(PF_3)_3(ads) + PF_3\uparrow(g)$).[25,26] This difference is, however, entirely consistent with the propensity for metal carbonyls to lose multiple CO ligands in a statistical process as a consequence of electronic excitation/ionization. ($M(CO)_n + e^- \rightarrow M(CO)_{n-x}^{+/-} + xCO_{(g)}\uparrow$; $x = 1, 2 \ldots n$).[23,24,65–69]

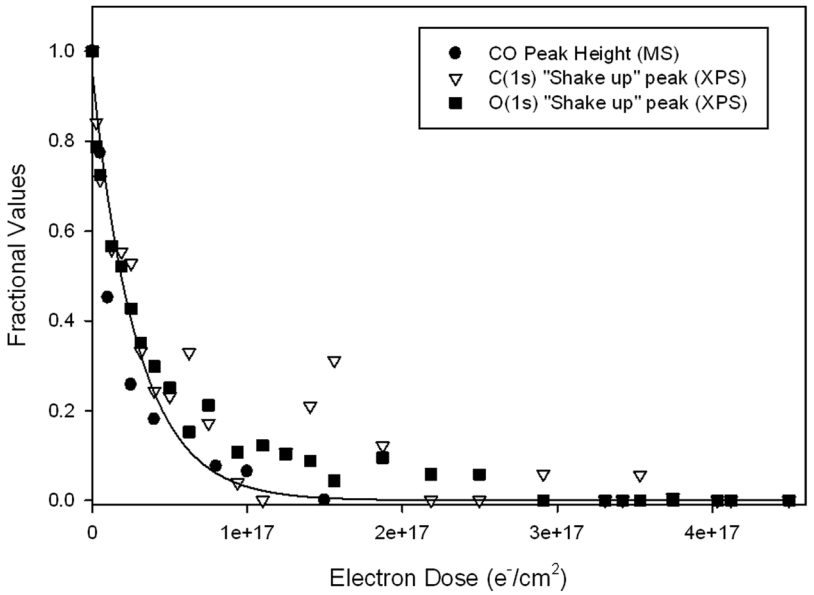

Fig. 8 Effect of electron dose on the fractional area of XPS shake-up peaks in the C(1s) (triangle) and O(1s) (square) regions, ratioed to the values observed on the same $W(CO)_6$ films prior to election irradiation. Also shown is the effect of electron dose on the fractional partial pressure of CO produced, ratioed to the value observed on a $W(CO)_6$ film of similar thickness, prior to election irradiation (circle).

Another important mechanistic question is whether the EBID process is initiated by the primary beam or the lower energy secondary electrons generated by the primary beam's interaction with the substrate. This issue is of relevance to EBID because it influences the ultimate size limitation/resolution with which nanostructures can be created.[70] If deposition is initiated by the primary beam (500 eV) then the reaction will be expected to proceed predominantly *via* electron ionization ($M(CO)_n + e^- \rightarrow M(CO)_n^+ \rightarrow$) while low energy electron (<10 eV) processes occur predominantly *via* dissociative electron attachment (DEA) and the subsequent dissociation of the transient negative ion formed ($M(CO)_n + e^- \rightarrow M(CO)_n^- \rightarrow$). Matejčík *et al.* have recently explored the product partitioning that characterizes both the low energy electron DEA and higher energy electron ionization processes of gas phase $W(CO)_6$.[23,24] In summary, these studies showed that electron ionization occurs with a threshold of around 40 eV and produces W^+, $W(CO)^+$ and $W(CO)_3^+$ as the most abundant three species. In contrast, dissociative electron attachment yields $W(CO)_5^-$, $W(CO)_4^-$ and $W(CO)_3^-$ as the predominant species. Our studies on surface bound $W(CO)_6$ molecules indicate that the average stoichiometry of the partially decarbonylated species formed by the initial electron decomposition event is $\approx W(CO)_4$ following the loss, on average of two CO groups. This is very much in line with the expectation of a low energy DEA step[24] as opposed to electron ionization, where gas phase studies would suggest an average loss of at least four CO molecules.[23] The similar changes in the C(1s) and O(1s) regions for $W(CO)_6$ films exposed to either electrons (Fig. 3) or X-rays (Fig. S1, ESI†) is also consistent with a process dominated by reactions involving low energy secondary electrons. In further support of the idea that it is low energy electron processes which predominate in EBID, recent studies on $MeCpPtMe_3$ and $Pt(PF_3)_4$ have shown a consistency between the dominant gas phase DEA processes[21,71] and the initial bond breaking process observed when the same molecules are adsorbed on solid surfaces and exposed to 500 eV electrons.[25,26] It is important to note, however, that the loss of two CO ligands per $W(CO)_6$ molecule represents an average value and that the statistical loss of CO groups from $W(CO)_6$ as a result of electron exposure means that the surface will in fact consist of a mixture of partially decarbonylated species with W : CO ratios of 1 : 5, 1 : 4, 1 : 3 *etc.* after the first step. The formation of a range of decarbonylated species, rather than one discrete product is also the reason why the IR intensity observed below 1950 cm^{-1} during electron exposure (Fig. 2) is somewhat broad and featureless, analogous to the observation of Hauchard and Rowntree during the electron irradiation of $Fe(CO)_5$ adsorbed on Au(111).[33]

Stage 2: electron stimulated decomposition of partially decarbonylated $W_x(CO)_y$ species

As a consequence of the initial step, where multiple (2–2.5) CO ligands are ejected from the parent molecule, partially decarbonylated $W_x(CO)_y$ species are created. It should be noted that we refer to these intermediates as $W_x(CO)_y$ rather than $W(CO)_y$ species due to the ability of metal carbonyls to form polynuclear metal carbonyl clusters,[72] although we have no direct experimental evidence to prove or refute this possibility in the present study.

Support for the idea that these $W_x(CO)_y$ species are formed can be found in the RAIR spectra in Fig. 2, particularly the appearance of spectral intensity just below 1950 cm^{-1}. The XPS data shown in Fig. 3(b) also supports the idea that $W_x(CO)_y$ species are formed. Thus, after an electron dose of 9×10^{16} e^- per cm^2

peaks at 286.4 and 533.1 eV in the C(1s) and O(1s) regions that can be associated with adsorbed CO molecules persist, even though the shake up features have disappeared. In previous studies we have shown that these peaks in the C(1s) and O(1s) regions disappear only when the substrate temperature is increased above 298 K. This behavior is consistent with the thermal stability of CO groups reported for other partially decarbonylated metal carbonyls created by electron irradiating $Ni(CO)_4$ and $Fe(CO)_5$.[32,34,38] In contrast, $W(CO)_6$ thermally desorbs under UHV conditions at $\approx$240 K.[73] One apparent inconsistency with the production of $W_x(CO)_y$ species is the lack of any shake up features associated with these moieties. However, previous studies have shown that for CO species, the intensity of shake up features in the O(1s) and C(1s) regions are often significantly more pronounced when the CO groups are present in the highly symmetric and molecularly well-defined environment of a hexacarbonyl.[59,74,75] For example, the O(1s) shake up feature of $W(CO)_6$ is $\approx$30% of the intensity of the main CO peak, while for CO adsorbed on a W surface the same feature is less than $<$10% of the main CO peak. We believe that it is a combination of the decrease in intensity of the shake up features for $W_x(CO)_y$ species, coupled with the range of different $W_x(CO)_y$ species that are produced (*e.g.* $W(CO)_5$, $W(CO)_4$, $W(CO)_3$ *etc.*) which causes the shake up features of these species to be too weak to be observed.

Once formed, the fate of $W_x(CO)_y$ species under the influence of electron irradiation differs markedly from that of the parent $W(CO)_6$ molecules. Specifically, our experimental data indicates that the $W_x(CO)_y$ species undergo ligand induced decomposition rather than desorption, forming oxidized tungsten atoms embedded in a carbonaceous matrix, thus:

$$W_x(CO)_y \xrightarrow{e^-} W_xO_y + C_{ads}$$

The most direct evidence for this process comes from the XPS data in Fig. 3(b), which shows that the W(4f), C(1s), and O(1s) regions evolve as the electron dose increases in excess of 9.36×10^{16} e^- per cm^2, at a point where Fig. 8 reveals that no more CO is evolved into the gas phase. RAIR data in Fig. 2 also supports the idea that these partially decarbonylated species are created and then subsequently decomposed by electron irradiation. Moreover, changes in the C(1s) and O(1s) regions indicate a conversion of CO species to graphitic like carbon and oxide (O^{2-}) species, indications of ligand decomposition ($CO(ads) + e^- \rightarrow C(ads) + O^{2-}(ads)$). We cannot discount the possibility that a small amount of the graphitic like carbon originates from hydrocarbon adsorption from the background (*i.e.* the electron gun). However, the observation that the fate of the oxygen and carbon atoms observed by XPS in Fig. 3 follow similar trends indicates that the majority of the graphitic carbon originated from the CO ligands in $W(CO)_6$. This assertion is also supported by the similar evolution of the C(1s) region during X-ray and electron irradiation (compare Fig. 3(a) and Fig. S1, ESI†), specifically the appearance of graphitic carbon following the loss of CO ligands associated with $W(CO)_6$ molecules.

Analysis of Fig. 3(b) and Fig. 5 reveal that the appearance of WO_3 is also observed for electron doses in excess of 9.36×10^{16} e^- per cm^2. This correlation between changes in the W(4f) region and the appearance of significant oxide species in the O(1s) regions is consistent with the idea that tungsten oxidation is initiated by reactions between reactive oxygen species (ions, radicals) formed by the electron stimulated decomposition of the CO ligands in $W_x(CO)_y$ species, and tungsten atoms.

Scheme 1 summarizes the electron induced surface processes that accompany the deposition of tungsten from $W(CO)_6$ as they relate to typical EBID experiments conducted under steady-state deposition conditions. The first step involves equilibration between gas phase and surface adsorbed $W(CO)_6$.[12–15] Our research indicates that deposition is initiated by the interactions of low energy secondary electrons (generated by the primary beam) and adsorbed $W(CO)_6$ molecules, forming a transient negative ion which then fragments into a partially decarbonylated $W_x(CO)_y$ species as CO ligands are ejected into the gas phase. Since the fragmentation of $W(CO)_6^-$ is a statistical process, a range of $W_x(CO)_y$ species will be formed. Under the influence of continued electron irradiation the fate of these $W_x(CO)_y$ species is characterized by ligand decomposition and the formation of tungsten oxides and graphitic carbon. The overall deposition mechanism outlined in Scheme 1 is in essence similar to the two step model proposed by Hoyle *et al.*, which was based on observations of EBID deposits

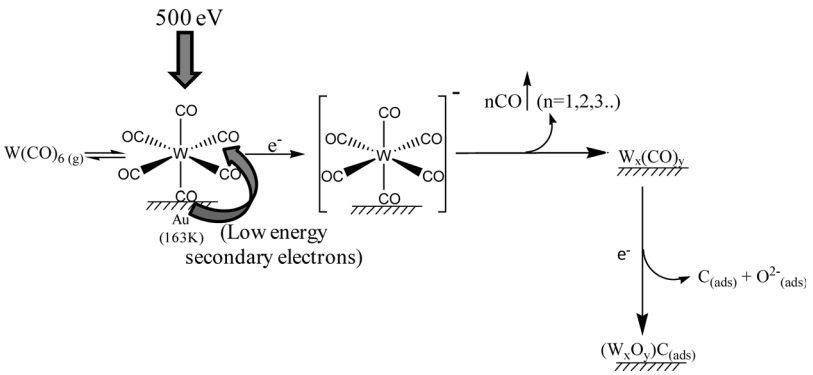

Scheme 1 Surface reactions responsible for electron beam induced decomposition of $W(CO)_6$.

created from $W(CO)_6$ under different conditions.[76] In this model the first step involves fragmentation of the precursor to create an intermediate, which can then react further to yield the final product. The overall reaction sequence can be considered to be a consequence of the different fate of the CO ligands which depends on their local environment:

$$CO_{(ads)} \rightarrow CO_{(g)} - \text{electron stimulated CO desorption from } W(CO)_6$$

$$CO_{(ads)} \rightarrow C_{(ads)} + O - \text{electron stimulated CO decomposition from } W_x(CO)_y \text{ species}$$

This idea is analogous to the one used by Foord and Jackman to describe the electron stimulated reactions of adsorbed $Fe(CO)_5$.[37] Our data suggests that most of the reactive oxygen species produced as a result of CO decomposition go on to oxidize tungsten atoms, although some could react with remaining CO species, which may account for the CO_2 observed in Fig. 7.

The initial step described in stage 1 represents the elementary bond breaking process that converts transiently adsorbed gas phase $W(CO)_6$ molecules into non-volatile surface bound species. Consequently, we can determine the reaction/deposition cross-section for 500 eV incident electrons ($\sigma_{W(CO)_6}$) by measuring the loss of the parent species as a function of the electron dose shown in Fig. 8. Based on the measured rate constant determined from Fig. 8 and the size of the sample (1 cm^2), $\sigma_{W(CO)_6} = 6.5 \times 10^{-16}$ cm^{-2}, an intermediate value between the reaction cross-sections previously determined for $MeCpPtMe_3$ (2.2×10^{-16} cm^2)[26] and $Pt(PF_3)_4$ (2.5×10^{-15} cm^{-2})[25] for 500 eV incident electrons and comparable to the cross-section observed for other surface bound metal carbonyls such as $Ni(CO)_4$ ($\sigma_{Ni(CO)_4} = 2 \times 10^{-16}$ cm^{-2} for incident electrons in the range 100–300 eV).[32]

In EBID, deposition is often performed in electron microscopes where the vacuum environment contains contaminant gases, specifically hydrocarbons and water vapor.[3,77–80] Consequently, these species can also be transiently adsorbed on the surface along with the precursor molecules, and their presence could influence the nature/composition of the deposit. To simulate this effect we conducted the experiment described in Fig. 6, where H_2O was co-adsorbed with $W(CO)_6$ and the mixture subsequently exposed to an electron dose (4.50×10^{17} e^- per cm^2) sufficient to cause all of the CO ligands to react (see Fig. 3). Analysis of Fig. 6 clearly shows that the presence of co-adsorbed water increases the fraction of WO_3 molecules created. This effect can be ascribed to the reactions of adsorbed water molecules or the reactive oxygen species (mostly like oxygen atoms or ions) formed by electron stimulated decomposition of water, with the tungsten atoms that are formed as a consequence of electron stimulated $W(CO)_6$ decomposition.

The results presented in this study provide a basis to understand the purely electron stimulated reactions of the precursor molecules. However, for nanostructures created in electron microscopes under steady state deposition conditions other factors must also be considered. This includes the effects of contaminant gases, whose influence on ultimate film composition is highlighted in Fig. 6. Another factor is the effect that substrate temperature can play in determining reaction pathways. Thus, in the case of $W(CO)_6$ the $W_x(CO)_y$ species formed in the deposition event can undergo thermally activated CO desorption/decomposition ($W_x(CO)_y + \Delta \rightarrow W + CO\uparrow$ and $W_x(CO)_y + \Delta \rightarrow W_xC_yO_z$) at temperatures only slightly above 298 K.[81] Consequently, depending on the power density being used during the deposition it is possible that thermal as well as electron stimulated processes will contribute to the fate of reaction intermediates. This is an important point because only the initial step in the reaction of an EBID precursor must be electron driven. Indeed, we believe that the onset of thermally activated CO desorption from $W_x(CO)_y$ species is the reason why Mulders *et al.* observed a significant increase in the tungsten content of EBID structures created from $W(CO)_6$ when the substrate temperature was increased from 25 to 150 °C.[82] Similarly, we believe that beam induced local heating and the onset of thermal reactions for intermediates such as $W_x(CO)_y$ species is one of the reasons why nanostructures formed in electron microscopes with more focused beams are often observed to contain higher metal content.[3,5] For example, at low electron beam powers Huth *et al.* observed W-metal contents for EBID nanostructures created from $W(CO)_6$ that are comparable to what we observed in the present UHV surface science study. As the electron power increased the %W in the deposits increased steadily as both the % carbon and oxygen content decreased at comparable rates to one another.[3] These observations are consistent with the idea that as electron power increases so does the relative importance of thermally assisted CO desorption from the partially decarbonylated $W_x(CO)_y$ species produced in the initial deposition event.

Conclusions

The electron stimulated reactions of surface adsorbed $W(CO)_6$ molecules proceeds in two discrete steps; ligand desorption followed by ligand decomposition following an overall pattern of reactivity that is consistent with the behavior of two other recently studied EBID precursors ($MeCpPtMe_3$ and $Pt(PF_3)_4$).[25,26] The most significant difference with $W(CO)_6$ is the loss of multiple ligands (2–2.5 CO groups) during the initial step in contrast to the cleavage of only one Pt–CH_3 and Pt–PF_3 bond for adsorbed $MeCpPtMe_3$ and $Pt(PF_3)_4$, respectively. For $W(CO)_6$, the loss of multiple CO groups leads to the formation of partially decarbonylated $W_x(CO)_y$ species which then undergo electron stimulated decomposition rather than desorption. The decomposition of CO ligands in the second step yields a mixture of tungsten oxides and residual carbon while the presence of co-adsorbed water enhances the degree of tungsten oxidation. In the context of typical EBID studies, this UHV surface science approach identifies the elementary bond breaking process responsible for deposition and also highlights the fact that some of the carbon and oxygen atom

impurities typically observed in nanostructured deposits created from $W(CO)_6$ originate from decomposition of the ligand architecture.

References

1 P. C. Hoyle, J. R. A. Cleaver and H. Ahmed, *J. Vac. Sci. Technol., B*, 1996, **14**, 662–673.
2 H. W. P. Koops, R. Weiel, D. P. Kern and T. H. Baum, *J. Vac. Sci. Technol., B*, 1988, **6**, 477–481.
3 F. Porrati, R. Sachser and M. Huth, *Nanotechnology*, 2009, **20**, 195301.
4 P. D. Rack, S. Randolph, Y. Deng, J. Fowlkes, Y. Choi and D. C. Joy, *Appl. Phys. Lett.*, 2003, **82**, 2326–2328.
5 I. Sychugov, Y. Nakayama and K. Mitsuishi, *J. Phys. Chem. C*, 2009, **113**, 21516–21519.
6 W. F. van Dorp, B. van Someren, C. W. Hagen, P. Kruit and P. A. Crozier, *J. Vac. Sci. Technol., B*, 2006, **24**, 618–622.
7 K. T. KohlmannvonPlaten, L. M. Buchmann, H. C. Petzold and W. H. Brünger, *J. Vac. Sci. Technol., B*, 1992, **10**, 2690–2694.
8 M. Tanaka, M. Shimojo, M. Han, K. Mitsuishi and K. Furuya, *Surf. Interface Anal.*, 2005, **37**, 261–264.
9 W. F. van Dorp, C. W. Hagen, P. A. Crozier and P. Kruit, *Nanotechnology*, 2008, **19**, 225305.
10 M. Han, K. Mitsuishi, M. Shimojo and K. Furuya, *Philos. Mag.*, 2004, **84**, 1281–1289.
11 P. C. Hoyle, J. R. A. Cleaver and H. Ahmed, *Appl. Phys. Lett.*, 1994, **64**, 1448–1450.
12 W. F. van Dorp and C. W. Hagen, *J. Appl. Phys.*, 2008, **104**, 081301.
13 S. J. Randolph, J. D. Fowlkes and P. D. Rack, *Crit. Rev. Solid State Mater. Sci.*, 2006, **31**, 55–89.
14 I. Utke, P. Hoffman and J. Melngailis, *J. Vac. Sci. Technol., B*, 2008, **26**, 1197–1276.
15 N. Silvis-Cividjian, C. W. Hagen, P. Kruit, M. A. v. d. Stam and H. B. Groen, *Appl. Phys. Lett.*, 2003, **82**, 3514–3516.
16 L. Frey, C. Lehrer and H. Ryssel, *Appl. Phys. A: Mater. Sci. Process.*, 2003, **76**, 1017–1023.
17 J. Y. Igaki, K. Kanda, Y. Haruyama, M. Ishida, Y. Ochiai, J. I. Fujita, T. Kaito and S. Matsui, *Microelectron. Eng.*, 2006, **83**, 1225–1228.
18 T. Fujii, K. Iwasaki, M. Muekane, T. Takeuchi, M. Hasuda, Y. Asahata, M. Kyohara, T. Kogure, Y. Kijima and T. Kaito, *J. Micromech. Microeng.*, 2005, **15**, S286–S291.
19 K. L. Klein, S. J. Randolph, J. D. Fowlkes, L. F. Allard, H. M. Meyer III, M. L. Simpson and P. D. Rack, *Nanotechnology*, 2008, **19**, 345705.
20 J. J. L. Mulders, L. M. Belova and A. Riazanova, *Nanotechnology*, 2011, **22**, 055302.
21 S. Engmann, M. Stano, S. Matejc and O. Ingolfsson, *Phys. Chem. Chem. Phys.*, 2012, **14**, 14611–14618.
22 S. Engmann, M. Stano, S. Matejcik and O. Ingolfsson, *Angew. Chem., Int. Ed.*, 2011, **50**, 9475–9477.
23 K. Wnorowski, M. Stano, W. Barszczewska, A. Jówko and Š. Matejčík, *Int. J. Mass Spectrom.*, 2012, **314**, 42–48.
24 K. Wnorowski, M. Stano, C. Matias, S. Denifl, W. Barszczewska and Š. Matejčík, *Rapid Commun. Mass Spectrom.*, 2012, **26**, 1–6.
25 K. Landheer, S. G. Rosenberg, L. Bernau, P. Swiderek, I. Utke, C. W. Hagen and D. H. Fairbrother, *J. Phys. Chem. C*, 2011, **115**, 17452–17463.
26 J. D. Wnuk, J. M. Gorham, S. G. Rosenberg, W. F. van Dorp, T. E. Madey, C. W. Hagen and D. H. Fairbrother, *J. Phys. Chem. C*, 2009, **113**, 2487–2496.
27 W. F. van Dorp, J. D. Wnuk, J. M. Gorham, D. H. Fairbrother, T. E. Madey and C. W. Hagen, *J. Appl. Phys.*, 2009, **106**, 074903.
28 J. D. Wnuk, J. M. Gorham, S. G. Rosenberg, T. E. Madey, C. W. Hagen and D. H. Fairbrother, *J. Vac. Sci. Technol., B*, 2010, **28**, 527–537.
29 J. D. Wnuk, J. M. Gorham, S. G. Rosenberg, W. F. van Dorp, T. E. Madey, C. W. Hagen and D. H. Fairbrother, *J. Appl. Phys.*, 2010, **107**, 054301.
30 J. D. Wnuk, S. G. Rosenberg, J. M. Gorham, W. F. van Dorp, C. W. Hagen and D. H. Fairbrother, *Surf. Sci.*, 2011, **605**, 257–266.
31 M. D. Xu and F. Zaera, *J. Vac. Sci. Technol., A*, 1996, **14**, 415–424.
32 R. D. Ramsier, M. A. Henderson and J. T. Yates, *Surf. Sci.*, 1991, **257**, 9–21.
33 C. Hauchard and P. A. Rowntree, *Can. J. Chem.*, 2011, **89**, 1163–1173.
34 M. A. Henderson, R. D. Ramsier and J. T. Yates, *Surf. Sci.*, 1991, **259**, 173–182.
35 Y. Wang, F. Gao, M. Kaltchev and W. T. Tysoe, *J. Mol. Catal. A: Chem.*, 2004, **209**, 135–144.
36 C. Hauchard, C. Pepin and P. Rowntree, *Langmuir*, 2005, **21**, 9154–9165.
37 J. S. Foord and R. B. Jackman, *Surf. Sci.*, 1986, **171**, 197–207.
38 M. A. Henderson, R. D. Ramsier and J. T. Yates, *J. Vac. Sci. Technol., A*, 1991, **9**, 1563–1568.
39 C. Hauchard, C. Pépin and P. Rowntree, *Langmuir*, 2005, **21**, 9154–9165.
40 S. J. Randolph, J. D. Fowlkes and P. D. Rack, *J. Appl. Phys.*, 2005, **97**, 124312.
41 P. A. Thiel and T. E. Madey, *Surf. Sci. Rep.*, 1987, **7**, 211–385.
42 S. Tanuma, C. J. Powell and D. R. Penn, *Surf. Interface Anal.*, 1991, **17**, 911–926.
43 J. J. T. Yates, *Experimental innovations in surface science: a guide to practical laboratory methods and instruments*, American Institute of Physics, 1998.
44 J. F. Moulder, *et al.*, *Handbook of x-ray photoelectron spectroscopy*, Physical Electronics USA, Inc., Chanhassen, 1995.
45 M. Suvanto and T. A. Pakkanen, *J. Mol. Catal. A: Chem.*, 1999, **138**, 211–220.
46 C. Stromberg, D. J. Myers and M. D. Fayer, *J. Chem. Phys.*, 2002, **116**, 3540–3553.
47 M. Broquier, C. Crepin, H. Dubost and J. P. Galaup, *Chem. Phys.*, 2007, **341**, 207–217.
48 R. N. Perutz and J. J. Turner, *Inorg. Chem.*, 1975, **14**, 262–270.

49 E. E. Platero and M. P. Mentruit, *Inorg. Chem.*, 1994, **33**, 1506–1509.
50 X.-Z. Sun, M. W. George, S. G. Kazarian, S. M. Nikiforov and M. Poliakoff, *J. Am. Chem. Soc.*, 1996, **118**, 10525–10532.
51 J. C. Cook and E. M. McCash, *Surf. Sci.*, 1996, **364**, L605–L611.
52 S. K. Clowes, E. A. Seddon and E. M. McCash, *Surf. Sci.*, 2000, **464**, L667–L672.
53 J. C. Cook and E. M. McCash, *Surf. Sci.*, 1996, **364**, L605–L611.
54 J. Jia, J. N. Kondo, K. Domen and K. Tamaru, *J. Phys. Chem. B*, 2001, **105**, 3017–3022.
55 W.-L. Yim, T. Nowitzki, M. Necke, H. Schnars, P. Nickut, J. Biener, M. Biener, V. Zielasek, K. Al-Shamery, T. Kluner and M. Baumer, *J. Phys. Chem. B*, 2007, **111**, 445–451.
56 C. J. Westgate, E. Lundgren, J. N. Andersen, E. D. L. Rienks, A. C. Gluhoi, J. W. Bakker, I. M. N. Groot and B. E. Nieuwenhuys, *Surf. Sci.*, 2009, **603**, 2152–2157.
57 R. N. Perutz and J. J. Turner, *J. Am. Chem. Soc.*, 1975, **97**, 4791–4800.
58 F. Zaera, *J. Phys. Chem.*, 1992, **96**, 4609–4615.
59 E. W. Plummer, W. R. Salenck and J. S. Miler, *Phys. Rev. B: Condens. Matter Mater. Phys.*, 1978, **18**, 1673.
60 X. Li, K. A. Wepasnick, X. Tang, Y. Wang, K. H. Bowen and D. H. Fairbrother, *J. Vac. Sci. Technol., B*, 2012, **30**, 031806.
61 C. Rincon, G. Zambrano, A. Carvajal, P. Prieto, H. Galindo, E. Martinez, A. Lousa and J. Esteve, *Surf. Coat. Technol.*, 2001, **148**, 277–283.
62 P. N. Ross and P. Stonehart, *J. Catal.*, 1977, **48**, 42–59.
63 J. Luthin and C. Linsmeier, *Surf. Sci.*, 2000, **454**, 78–82.
64 J. R. Swanson, F. A. Flitsch and C. M. Friend, *Surf. Sci.*, 1989, **215**, L293–L296.
65 D. R. Bidinosti and N. S. McIntyre, *Can. J. Chem.*, 1967, **45**, 641–648.
66 A. Foffani, B. Cantone, S. Pignataro and F. Grasso, *Z. Phys. Chem.*, 1965, **45**, 79–88.
67 S. Pignataro, A. Foffani, F. Grasso and B. Cantone, *Z. Phys. Chem.*, 1963, **47**, 106–113.
68 F. Qi, S. H. Yang, L. S. Sheng, H. Gao, Y. W. Zhang and S. Q. Yu, *J. Chem. Phys.*, 1997, **107**, 10391–10398.
69 R. E. Winters and R. W. Kiser, *Inorg. Chem.*, 1965, **4**, 157–161.
70 K. T. K. vonPlaten, J. Chlebek, M. Weiss, K. Reimer, H. Oertel and W. H. Brunger, *J. Vac. Sci. Technol., B*, 1993, **11**, 2219–2223.
71 O. May, D. Kubala and M. Allan, *Phys. Chem. Chem. Phys.*, 2012, **14**, 2979–2982.
72 F. A. Cotton and G. Wilkinson, *Advanced Inorganic Chemistry*, John Wiley & Sons, New York, 1980.
73 M. D. Xu and F. Zaera, *J. Vac. Sci. Technol., A*, 1996, **14**, 415–424.
74 E. Umbach, J. C. Fuggle and D. Menzel, *J. Electron Spectrosc. Relat. Phenom.*, 1977, **10**, 15–34.
75 J. T. Yates, T. E. Madey and N. E. Erickson, *Surf. Sci.*, 1974, **43**, 257–274.
76 P. C. Hoyle, J. R. A. Cleaver and H. Ahmed, *J. Vac. Sci. Technol., B*, 1996, **14**, 662–673.
77 F. Porrati, R. Sachser, C. H. Schwalb, A. S. Frangakis and M. Huth, *J. Appl. Phys.*, 2011, **109**, 063715.
78 A. Botman, C. W. Hagen, J. Li, B. L. Thiel, K. A. Dunn, J. J. L. Mulders, S. J. Randolph and M. Toth, *J. Vac. Sci. Technol., B*, 2009, **27**, 2759–2763.
79 A. Botman, M. Hesselberth and J. J. L. Mulders, *Microelectron. Eng.*, 2008, **85**, 1139–1142.
80 J. T. Li, M. Toth, K. A. Dunn and B. L. Thiel, *J. Appl. Phys.*, 2010, **107**, 103540.
81 S. G. Rosenberg, K. Landheer, C. W. Hagen and D. H. Fairbrother, *J. Vac. Sci. Technol., B*, 2012, **30**, 051805.
82 J. J. L. Mulders, L. M. Belova and A. Riazanova, *Nanotechnology*, 2011, **22**, 055302.